Talanta 82 (2010) 1044–1051

Contents lists available at ScienceDirect

Talanta

journal homepage: www.elsevier.com/locate/talanta

Enhanced oxygen sensing properties of Pt(II) complex and dye entrapped core–shell silica nanoparticles embedded in sol–gel matrix

Chen-Shane Chu, Yu-Lung Lo*, Ti-Wen Sung

Department of Mechanical Engineering, National Cheng Kung University, No. 1, Ta-Hsueh Road, Tainan, Taiwan

ARTICLE INFO

Article history:
Received 29 March 2010
Received in revised form 8 June 2010
Accepted 10 June 2010
Available online 23 June 2010

Keywords:
Optical fiber oxygen sensor
Pt(II) complex
Core–shell
Sol–gel process

ABSTRACT

This paper presents a highly sensitive oxygen sensor that comprises an optical fiber coated at one end with platinum(II) meso-tetrakis(pentafluorophenyl)porphyrin (PtTFPP) and PtTFPP entrapped core–shell silica nanoparticles embedded in an n-octyltriethoxysilane (Octyl-triEOS)/tetraethylorthosilane (TEOS) composite xerogel. The sensitivity of the optical oxygen sensor is quantified in terms of the ratio I_0/I_{100}, where I_0 and I_{100} represent the detected fluorescence intensities in pure nitrogen and pure oxygen environments, respectively. The experimental results show that the oxygen sensor has a sensitivity (I_0/I_{100}) of 166. The response time was 1.3 s when switching from pure nitrogen to pure oxygen, and 18.6 s when switching in the reverse direction. The experimental results show that compared to oxygen sensors based on PtTFPP, PtOEP, or $Ru(dpp)_3^{2+}$ dyes, the proposed optical fiber oxygen sensor has the highest sensitivity. In addition to the increased surface area per unit mass of the sensing surface, the dye entrapped in the core of silica nanoparticles also increases the sensitivity because a substantial number of aerial oxygen molecules penetrate the porous silica shell. The dye entrapped core–shell nanoparticles is more prone to oxygen quenching.

1. Introduction

Oxygen plays an essential role as either a reactant or a product in many chemical and biochemical reactions. Consequently, researchers have expended considerable effort in developing reliable techniques for the high-precision measurement of oxygen concentrations. One of the earliest oxygen sensors was the Clark electrode, designed to measure the oxygen pressure in arterial blood samples [1]. Although this sensor provides reasonably accurate measurement results, it has a number of drawbacks which limit its general applicability, most notably high oxygen consumption, a slow response time, poor reliability, and questionable safety [2]. Optical oxygen sensors effectively remove many of these limitations and have therefore found widespread use in chemical [3–8], clinical [9,10], and environmental [11] fields. Such sensors detect the oxygen concentration by monitoring the reduction in the fluorescence intensity of an excited fluorescent indicator as a result of the quenching effect induced by the oxygen environment. Optical oxygen sensors presented in the literature invariably embed the fluorescent indicator in either a polymer [12–15] or a sol–gel matrix [16–22]. Many researchers have reported that sol–gel derived glass is an ideal matrix material for oxygen sensing applications since it is highly permeable to oxygen and has favorable mechanical properties, excellent chemical stability, and superior optical clarity [23–25]. Furthermore, it has been shown that organically modified silicate (ORMOSIL) matrixes [16–22] improve the response and sensitivity of ruthenium-(II)-complex-based [17–19] and platinum-(II)-complex-based oxygen sensors [20–22] due to their porous structure, which enhances their ability to accommodate and disperse analyte-sensitive dyes.

Ruthenium(II) complexes have a number of advantages for optical oxygen sensing applications, including long excitation lifetimes (5.3 μs), good fluorescence quantum yields, and good oxygen quenching efficiency [26]. Compared to ruthenium(II) complexes, platinum phosphorescent porphyrins such as platinum tetrakis pentrafluoropheny porphine (PtTFPP) have many favorable characteristics, including a higher sensitivity to oxygen quenching, longer excitation and emission wavelengths, a more rapid response, a larger Stokes' shift (100–170 nm), and a higher photochemical stability [20–22]. Consequently, these platinum(II) complexes have been extensively used for oxygen sensor applications in recent years [20–22].

Although considerable progress has been made in the optical chemical sensing field in recent years, the development of ultrasensitive detection techniques still remains a major challenge. It is known that the sensitivity of sensors which detect the analyte of interest via its interaction with dye molecules embedded

* Corresponding author. Tel.: +886 6 2757575x62123; fax: +886 6 2352973.
E-mail address: loyl@mail.ncku.edu.tw (Y.-L. Lo).

0039-9140/$ – see front matter © 2010 Elsevier B.V. All rights reserved.
doi:10.1016/j.talanta.2010.06.020

in the sensing surface increases with increasing surface area per unit mass. Accordingly, various designs for chemical sensors with enlarged sensing surfaces have been proposed [27]. However, these sensors invariably involve sophisticated synthesis routes or require cumbersome fabrication processes. Therefore, a requirement for simple, low-cost approaches for the fabrication of ultra-sensitive detection systems still exists.

Recent studies have demonstrated the use of surface-modified core–shell nanoparticles in bio-analysis applications. Typically, the biomarkers constructed using this approach feature thin sensing shells incorporating core–shell silica nanoparticles for biological applications [28–30]. The core–shell silica nanoparticles can be synthesized using a simple process in which a silica precursor is used. Shells with a size in the range of a few nanometers [28] to hundreds of nanometers [31] can be synthesized. The core–shell silica particle membranes have a higher surface area than that of continuous thin films. This large available surface area has the potential to provide unusually high sensitivity in sensing applications. In a recent study, Han et al. [32] demonstrated an oxygen sensor based on a phosphorescent dye adsorbed in the pores of mesoporous silica nanoparticles deposited with sub-monolayer coverage on a layer-by-layer self-assembled film. Because of the high surface-to-volume ratio, a monolayer of micrometer-sized mesoporous silica nanoparticles can adsorb sufficient dye to produce a strong photoluminescence (PL) signal, and at the same time provide rapid access to oxygen molecules.

Dye entrapped core–shell silica nanoparticles are often used as bioimaging labels for living cells [33]. In the present study, an optical fiber oxygen sensor with the dye entrapped in the core of silica nanoparticles inside silica gels to enhance sensitivity is developed. The oxygen sensor is fabricated by coating one end of an optical fiber with a PtTFPP complex and dye entrapped core–shell silica nanoparticles embedded in an Octyl-triEOS/TEOS sol–gel matrix. In addition to the increased surface area per unit mass of the sensing surface, the dye entrapped in the core of silica nanoparticles also increases sensitivity. Silica nanoparticles without dye entrapped with PtTFPP embedded in an Octyl-triEOS/TEOS sol–gel matrix were fabricated for comparison.

2. Theory

Although luminophore quenching depends on several factors, in the simplest scenario of a luminophore in a homogeneous microenvironment, the quenching effect can be described by the Stern-Volmer equation [34]:

$$\frac{I_0}{I} = 1 + K_{SV}[O_2] \quad (1)$$

where I_0 and I represent the steady-state fluorescence intensities in the absence and presence, respectively, of the quencher (O_2 in the current case); K_{SV} is the Stern-Volmer quenching constant; $[O_2]$ is the oxygen concentration In the ideal case, a plot of I_0/I against $[O_2]$ is linear with a slope equal to K_{SV} and an intercept of unity, allowing the application of a simple single-point sensor calibration scheme.

Eq. (1) describes the idealized behavior of a luminophore with a single excited-state lifetime in a homogeneous environment undergoing dynamic quenching. The Stern-Volmer plot of fluorescence quenching of the sensors is nonlinear due to the presence of both static and dynamic quenching. Demas et al. reported a multi-site model for a sensing film with various oxygen-accessible sites [8,35,36]. In this model, the oxygen molecule can exist at various sites, each with its own characteristic quenching constant. Since the observed fluorescence intensity is the sum of emissions from all oxygen-accessible sites, the Stern-Volmer relationship is modified as [8,35,36]:

$$\frac{I_0}{I} = \left[\sum_{1}^{n} \frac{f_n}{1 + K_{SVn}[O_2]}\right]^{-1} \quad (2)$$

where f_n denotes the fractional contribution to the total emission from domain/site n and K_{SVn} is the Stern-Volmer quenching constant associated with domain/site n. The best fit in this situation using above equation for $n = 2$.

3. Experimental

3.1. Fabrication of two optical fiber oxygen sensors

The optical oxygen sensor developed in this study was fabricated using a platinum(II) complex (PtTFPP) and PtTFPP entrapped core–shell silica nanoparticles embedded in an n-octyltriethoxysilane (Octyl-triEOS)/tetraethylorthosilane (TEOS) composite xerogel. For comparison, silica nanoparticles (without a core–shell structure) with PtTFPP complex embedded in an Octyl-triEOS/TEOS composite xerogel were also fabricated for an optical oxygen sensor. The basic steps of these two fabrication procedures are described in the sub-sections below and are illustrated schematically in Figs. 1 and 2, respectively.

3.2. Synthesis of PtTFPP entrapped core–shell silica nanoparticles

The PtTFPP entrapped core–shell silica nanoparticles were prepared using a modified form of the Stöber method [37]. Briefly, PtTFPP/EtOH (1 mM, 1 mL) solution was dissolved in 1 mL of TEOS and the resulting solution was stirred for 10 min. Ammonium hydroxide (1 M, 0.78 mL) was then added to the PtTFPP/EtOH/TEOS solution, which was subsequently stirred for 1 h to obtain a completely homogeneous solution (designated as solution "A" in Fig. 1). A second solution (designated as solution "B" in Fig. 1) was prepared by adding 0.15 mL of TEOS to 7.5 mL of ethanol and then stirring for 10 min. Solution A was then slowly added to solution B and the resulting solution (solution "C") was stirred for 10 min. Ammonium hydroxide (0.185 mL) and water (0.785 mL) were added to solution C and the resulting solution was stirred for a further 3 h. TEOS (1.8 mL) and more ammonium hydroxide (1.17 mL) were then added to the solution, which was subsequently stirred for 15 h. Finally, the solution was centrifuged and the resulting precipitate was washed with acetone until a clear supernatant was obtained. Note that in preparing the PtTFPP entrapped core–shell silica nanoparticles using the process described above, all of the synthesis steps were performed at room temperature using a technique similar to that described by Ethiraj et al. [30].

3.3. Synthesis of silica nanoparticles

The silica nanoparticles were prepared using a simple method [38]. Briefly, the absolute ethanol (4.6 mL) solution was dissolved in 1 mL of ammonium hydroxide (13.7 M) and the resulting solution was stirred for 10 min (designated as solution "A" in Fig. 2). A second solution (designated as solution "B" in Fig. 2) was prepared by adding 0.1 mL of TEOS to 0.4 mL of absolute ethanol and then stirring for 10 min. Solution B was then quickly added to solution A and the resulting solution (solution "C") was stirred for 2 h. Finally, the solution was centrifuged and the resulting precipitate was washed with acetone until a clear supernatant was obtained.

3.4. Sol–gel, mixing, and dipping processes

The Octyl-triEOS/TEOS composite sol used as the matrix material in the proposed oxygen sensor was prepared by mixing

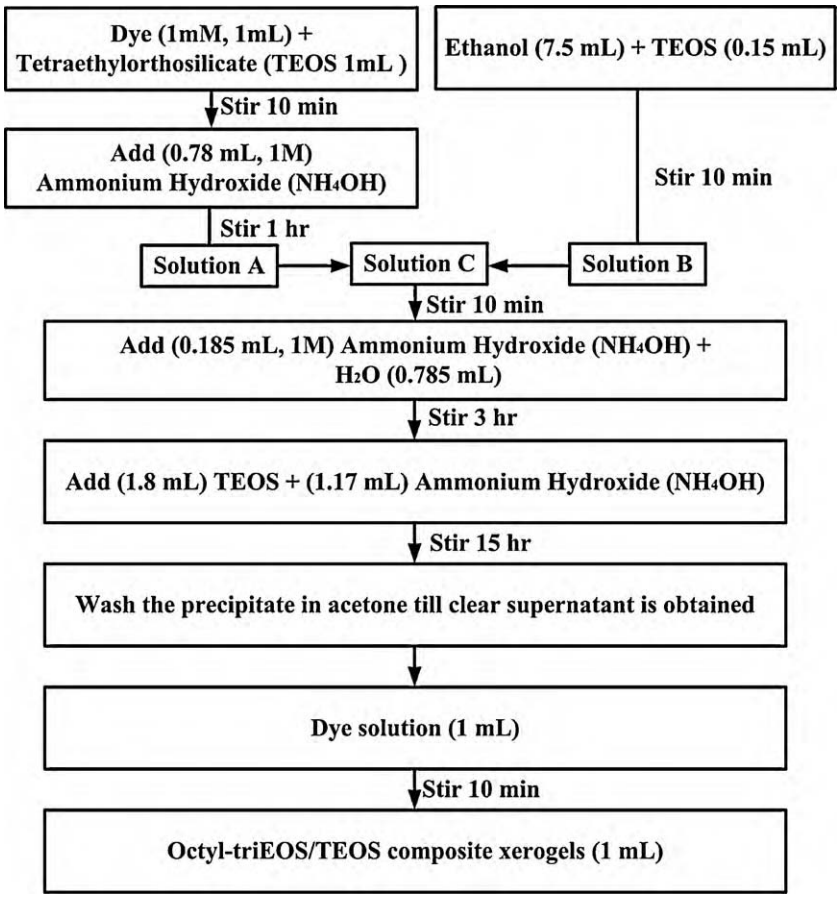

Fig. 1. Flow chart showing the basic synthesis procedure of fabricating composite xerogel with embedded PtTFPP and dye entrapped core–shell silica nanoparticles.

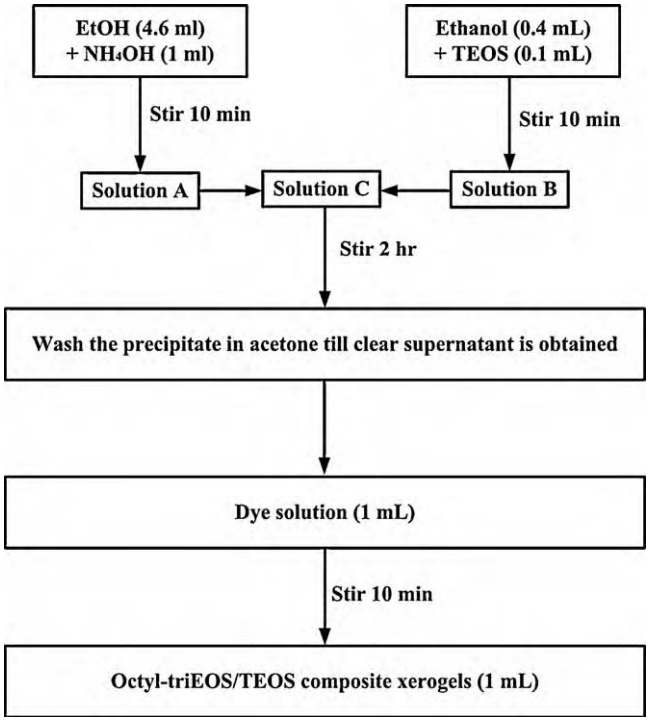

Fig. 2. Flow chart showing basic synthesis procedure of fabricating composite xerogel with embedded dye solution and silica nanoparticles.

Octyl-triEOS (0.2 mL) and TEOS (4 mL) to form a precursor solution. Adopting an approach similar to that employed by Yeh et al. [21], EtOH (1.25 mL) and HCl (0.1 M, 0.4 mL) were then added to the sol solution to catalyze the ORMOSIL reaction. The resulting solution was capped and stirred magnetically for 1 h at room temperature. During the mixing process, Triton-X-100 (0.1 mL) was added to the solution to improve the homogeneity of the silica sol, resulting in a crack-free monolith. The oxygen-sensitive dye solution was prepared by dissolving 2 mg of PtTFPP into 10 mL of EtOH. The resulting solution (1 mL) was then added to the PtTFPP entrapped core–shell silica nanoparticles or the silica nanoparticles and stirred for 10 min. The solution was then added to the composite sol solution. Finally, the solution was capped and stirred magnetically for another 10 min. The various sensor cocktails were prepared using a similar procedure; the compositions are given in Table 1.

The sensor fabrication process was commenced by soaking a multimode optical fiber in NaOH for 24 h. The fiber was then rinsed with copious amounts of de-ionized water and EtOH and then dried at room temperature for 10 min. The composite xerogel with the dye entrapped core–shell silica nanoparticles or the silica nanopar-

Table 1
Compositions of cocktails used as O_2-sensing materials.

Abbreviation	Dye in bulk matrix	Dye in core–shell beads	Silica nanoparticles
S-1	+	+	–
S-2	+	–	+
S-3	–	+	–

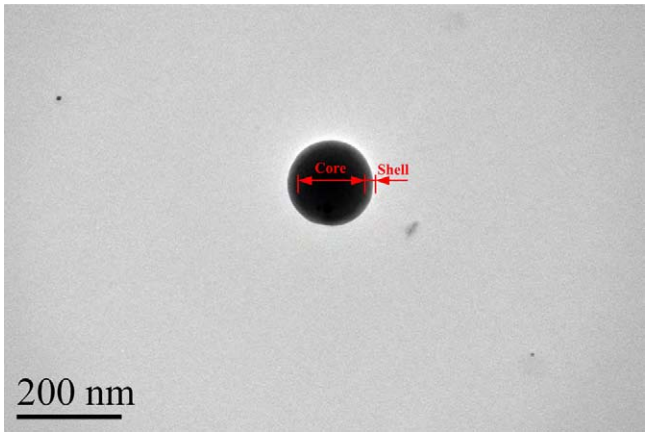

Fig. 3. TEM image showing a PtTFPP entrapped core–shell silica nanoparticle at a resolution of 200 nm.

ticles was then deposited on one end of the fiber in a dip-coating operation performed at a velocity of 0.25 mm/s. Finally, the coated fiber was dried at room temperature and left to stabilize under ambient conditions for 1 week. A flow chart showing the basic synthesis procedure of fabricating composite xerogel with embedded PtTFPP and dye entrapped core–shell silica nanoparticles is illustrated in Fig. 1. A flow chart showing basic synthesis procedure of fabricating composite xerogel with embedded dye solution and silica nanoparticles is illustrated in Fig. 2.

3.5. Characteristics of silica nanoparticles and PtTFPP entrapped core–shell silica nanoparticles

Fig. 3 shows a TEM image of a PtTFPP entrapped core–shell silica nanoparticle synthesized using the processing steps described above. It can be seen that the PtTFPP entrapped core–shell silica nanoparticles are spherical with a diameter of around 170 nm. The core–shell structure can be observed clearly due to the different electron penetrabilities for the core and shell. The core is a black sphere with an average size of 145 nm (in diameter), and the shell is gray with an average thickness of 12.5 nm. These results are consistent with those of Wang et al. [39].

Fig. 4 shows a TEM image of silica nanoparticles. The silica nanoparticles are spherical with a diameter of around 400 nm. The TEM samples were prepared by dropping 5 μL of ethanol solution with nanoparticles on ultrathin 400 mesh copper grids. The copper grids were dried in an oven for 2 h at 110 °C and ready for TEM analyses after the copper grids were cooled to room temperature.

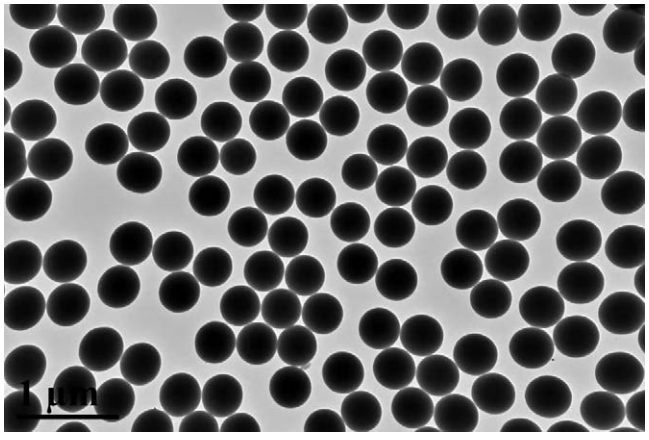

Fig. 4. TEM image showing silica nanoparticles at a resolution of 1 μm.

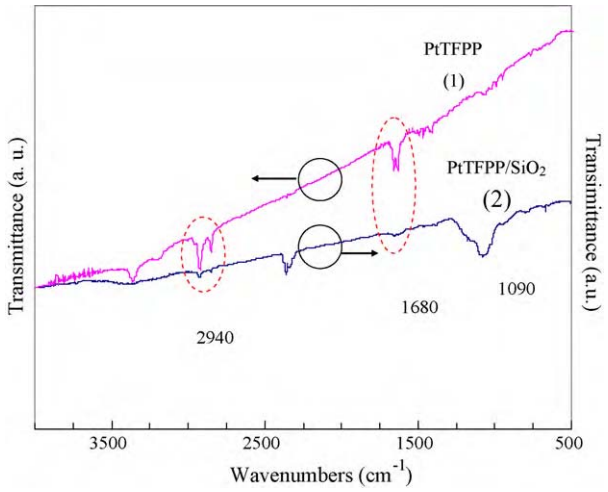

Fig. 5. FTIR spectra of (1) PtTFPP and (2) PtTFPP/SiO_2.

From Figs. 3 and 4, it is expected that this large available surface area will provide unusually high sensitivity in sensing applications.

Fig. 5 shows the FTIR spectra of the dye and the dye entrapped core–shell silica nanoparticles. The characteristic absorptions of PtTFPP (curve 1) were observed at 1680 cm^{-1} and 2490 cm^{-1}. For PtTFPP/SiO_2 core–shell nanoparticles (curve 2), the sharp band at 1090 cm^{-1} corresponds to Si–O–Si antisymmetric stretching vibrations, indicating the existence of SiO_2 in the nanoparticles. In the spectrum of PtTFPP/SiO_2 core–shell nanoparticles (curve 2), this suggests that PtTFPP is doped in the silica core of the composite core–shell nanoparticles. These results are consistent with of Chang et al. [40]. Additionally, the photophysical characteristics of core–shell fluorescent silica nanoparticles have been reported by the Refs. [29,30,39]. For example, Ow et al. [29] showed the core–shell nanoparticles are monodisperse in solution, 20 times brighter, and more photostable than their fluorophore and are amenable to specific labeling of biological macromolecules for biomaging experiments. On the other hand, Ethiraj et al. [30] presented the photoluminescent core–shell particles of organic dye in silica. The photoluminescence investigations showed that highly luminescent and photostable core–shell particles are formed and the core–shell particles can be easily suspended in water and would be useful for a variety of applications. Based on the photophysical characteristics, we hypothesized the dye entrapped core–shell particles in the optical oxygen sensor could result in the high surface-to-volume ratio to enhance the sensitivity of these optical fiber oxygen sensors. In addition to the increased surface area per unit mass in the sensing surface, the dye entrapped in the core of silica particles also play a role in the increased sensitivity because of the penetration of substantial amount aerial oxygen molecules through the porous silica shell [32].

3.6. Instrumentation

Fig. 6 shows a schematic illustration of the experimental arrangement used to characterize the performance of the optical fiber oxygen sensor. In the sensing experiments, the fluorescence excitation was provided by an LED (LED405E, Thorlabs) with a central wavelength of 405 nm driven by an arbitrary waveform generator (TGA1240, Thurlby Thandar Instruments (TTI) Ltd.) at 10 kHz. The oxygen sensing system consisted of a coated multimode silica glass fiber (1000/1035 μm) and a bifurcated optical fiber (BIF-600-UV-VIS, Ocean Optics). The emission measurements were acquired at a pressure of 101.3 kPa using a USB 2000 spectrometer (Ocean Optics).

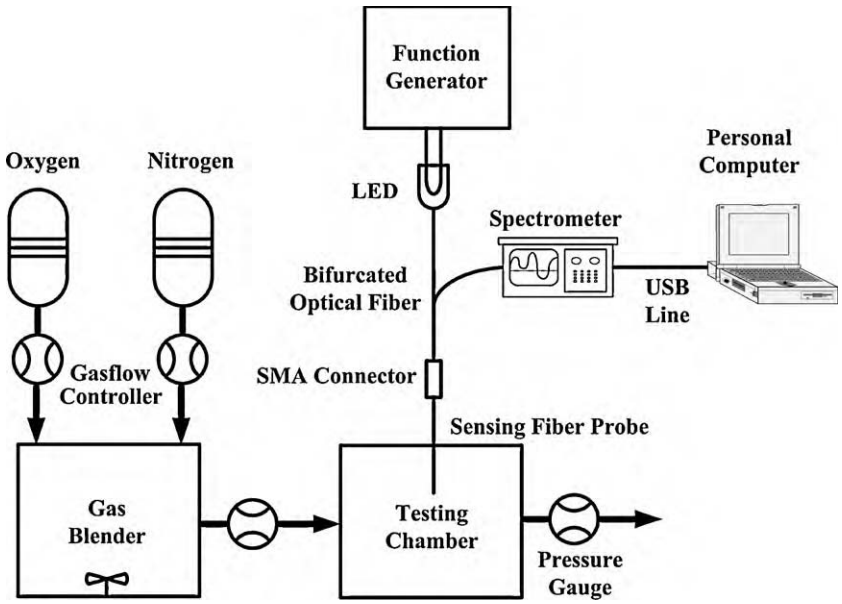

Fig. 6. Schematic diagram showing experimental arrangement used for characterization purposes.

4. Results and discussion

4.1. Optical properties of PtTFPP-doped sensor

Fig. 7 shows the absorption spectrum of the proposed PtTFPP-doped oxygen sensor. As shown, the spectrum has a Soret band at 392 nm and two Q bands at 508 nm and 541 nm, respectively. The experimental results confirm that the LED with a central wavelength of 405 nm is a suitable excitation source for the proposed sensor.

4.2. Oxygen sensing properties of PtTFPP-doped sensors

Figs. 8 and 9 show the variation of I_0/I with oxygen concentration for two PtTFPP-doped oxygen sensors, respectively. Figs. 8(a) and 9(a) reveal that the sensors exhibit a nonlinear response at high oxygen concentrations. It can be seen that the two PtTFPP-doped oxygen sensors have overall sensitivities of 166 (S-1) and 106 (S-2), respectively. The sensitivity of the optical oxygen sensor is quantified in terms of the ratio I_0/I_{100}, where I_0 and I_{100} represent the detected fluorescence intensities in pure nitrogen and pure oxygen environments, respectively. In Figs. 8(a) and 9(a), the solid line is the best-fit curve obtained using Eq. (2) ($n = 2$). There are two types of oxygen-accessible site in the sensing film; one is readily accessible to oxygen ($K_{SV1} = 5.1154\%^{-1}$, $f_1 = 0.9957$ for Fig. 8(a); $K_{SV1} = 1.6965\%^{-1}$, $f_1 = 0.9963$ for Fig. 9(a) (dynamic quenching site)) and the other is less accessible to oxygen ($K_{SV2} = 0.0005\%^{-1}$, $f_2 = 0.0043$ for Fig. 8(a); $K_{SV2} = 0.00004\%^{-1}$, $f_2 = 0.0037$ for Fig. 9(a) (static quenching site)). K_{SV2} has a very low value and makes a small contribution compared to that of K_{SV1},

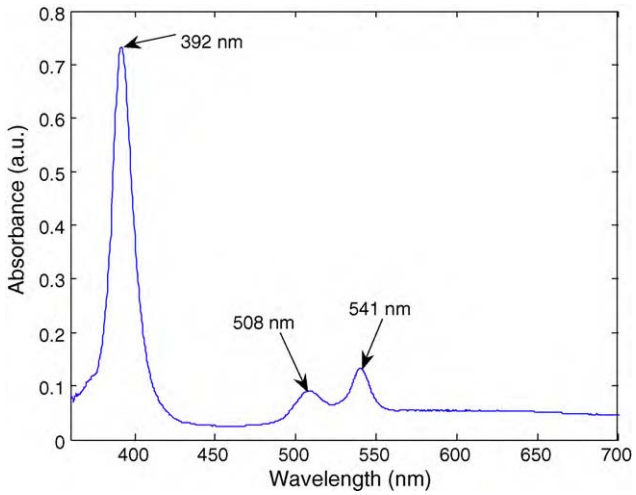

Fig. 7. Absorption spectrum of PtTFPP-doped oxygen sensor.

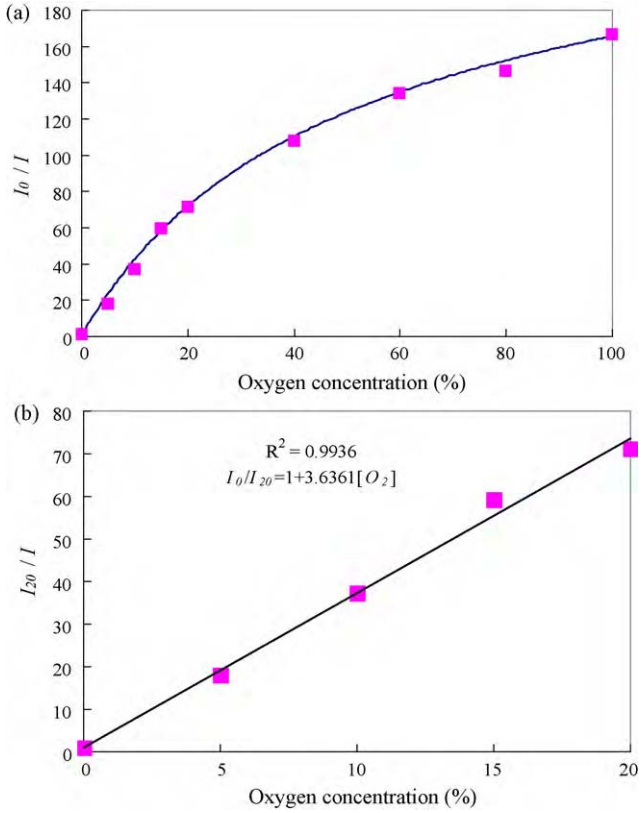

Fig. 8. Stern-Volmer plot of PtTFPP-doped dye entrapped core–shell silica particle oxygen sensor (S-1) for oxygen concentrations in ranges of (a) 0–100% and (b) 0–20%.

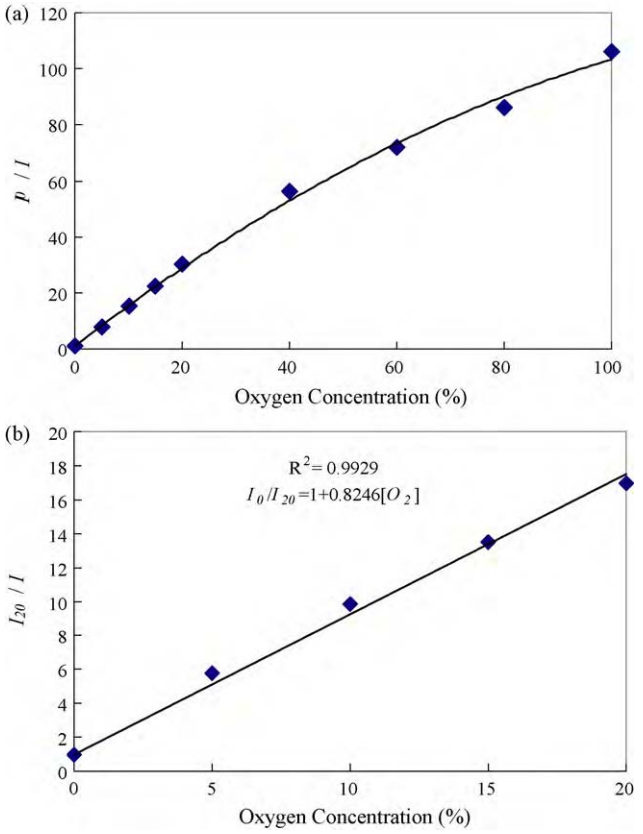

Fig. 9. Stern-Volmer plot of PtTFPP-doped silica particle oxygen sensor (S-2) for oxygen concentrations in ranges of (a) 0–100% and (b) 0–20%.

indicating that the oxygen-accessible site is a dynamic quenching site of the PtTFPP sensing film. The static quenching site is probably due to the core–shell nanoparticles.

The optical fiber oxygen sensors in the system are based on the collisional quenching of the dye molecule embedded in a porous support matrix with oxygen. The quenching process of the optical fiber oxygen sensors at low oxygen concentration, shown in Figs. 8(b) and 9(b), can be described by the Stern-Volmer equation (Eq. (1)). The figures demonstrate that the two PtTFPP-doped oxygen sensors have good linear responses with overall sensitivities of 70 and 30, respectively, in oxygen concentrations ranging from 0 to 20% and consequently showed the $K_{SV} = 3.6361\%^{-1}$ and $0.8246\%^{-1}$ for Figs. 8(b) and 9(b), respectively.

The sensor (S-3) properties of the sol–gel matrix incorporating PtTFPP-doped core–shell nanoparticles without dye solution were tested at various oxygen concentrations; the results are shown in Fig. 10. In the figure, the data indicate that the material responses to oxygen. The solid line in Fig. 10 is the best-fit curve obtained using Eq. (2) ($n = 2$). When O_2-sensitive PtTFPP is encapsulated inside the silica core and incorporated with a sol–gel matrix, fluorescence quenching and sensitivity can be observed. This is due to O_2 having a large membrane permeability constant, allowing substantial transport across the bilayer via simple diffusion [41]. Santra et al. [42] described a fluorescence lifetime-based approach for determining the core–shell nanostructure of FITC-(fluorescein isothiocyanate, isomer I) doped fluorescent silica nanonanoparticles (FSNPs). Their optical approach not only reveals the core–shell nanostructure of FSNPs but can also be used to evaluate the photobleaching of FSNPs in both solvated and non-solvated (dry) states. In the dry state, the dye doped fluorescence silica nanonanoparticles showed photobleaching, which was explained by a substantial number of aerial oxygen molecules penetrating the porous silica

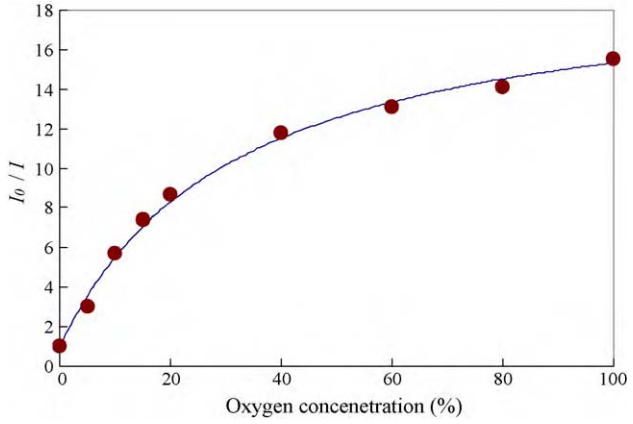

Fig. 10. Stern-Volmer plot of PtTFPP-doped silica particle oxygen sensor (S-3) without dye solution for oxygen concentrations in the range of 0–100%.

shell [43]. Microporous silica spheres were synthesized by Vacassy et al. using the same Stöber method. The nanoparticles were microporous and the specific surface area of the nanoparticles was very high [43]. Again, due to the porosity, the oxygen molecules penetrated into the microporous silica spheres.

In the present study, the adsorption average pore width (4 V/A by BET) of core–shell nanoparticles is 15.4 nm. Therefore, the Branouer, Emmet, and Teller (BET) specific surface area of the core–shell nanoparticles is 0.69 m^2/g. The pore width and specific surface area show that the dye entrapped core–shell nanoparticles are porous. As a result, the oxygen molecules can penetrate into the dye entrapped core–shell nanoparticles. The Stern-Volmer plot is shown in Fig. 10.

Fig. 11 shows the effects of aging time on the O_2 sensors' response stability. Initially, the PtTFPP-doped dye entrapped core–shell silica particle oxygen sensor (S-1) has the greatest sensitivity (I_0/I_{100}); however, as the sensor ages, the sensitivity decreases by almost 25% ($I_0/I_{100} = 166$ at 1 week and $I_0/I_{100} = 125$ at 8 weeks). Thus, the PtTFPP-doped dye entrapped core–shell silica particle oxygen sensor (S-1) loses sensitivity with time. The PtTFPP-doped silica particle oxygen sensor (S-2) has better stability. This is due to a substantial number of aerial oxygen molecules penetrating the porous silica shell, causing dye photobleaching [42].

4.3. Response time of PtTFPP-doped sensors

Fig. 12(a) and (b) shows the dynamic response of the PtTFPP-doped dye entrapped core–shell silica particle and PtTFPP-doped

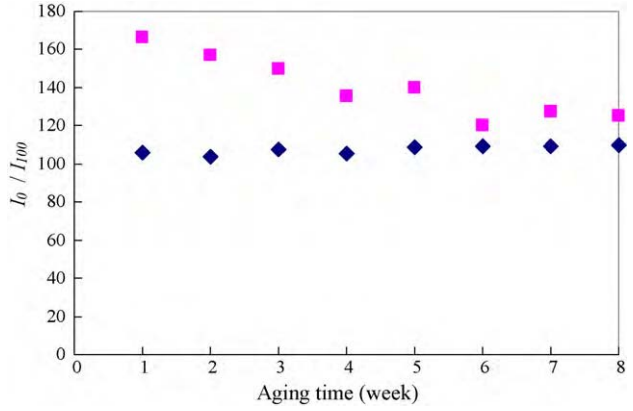

Fig. 11. Effects of aging on the average response stability for (■) PtTFPP-doped dye entrapped core–shell silica particle (□) PtTFPP-doped silica particle oxygen sensors.

Table 2
Comparison of performance characteristics of the proposed oxygen sensor with those of existing optical oxygen sensors.

Oxygen-sensitive dye	Support matrix	Response time	I_{N_2}/I_{O_2}	Refs.
$Ru(dpp)_3^{2+}$	TEOS	0% O_2 to 100% O_2: 3.5 s 100% O_2 to 0% O_2: 30 s	12	[17]
$Ru(dpp)_3^{2+}$	Octyl-triEOS/TEOS	None	16.5	[18]
$Ru(dpp)_3^{2+}$	n-Propyl-TriMOS/TFP-TriMOS	Sensors response times were <5 s	35	[19]
PtTFPP	Octyl-triEOS/TEOS	0% O_2 to 100% O_2: 0.6 s 100% O_2 to 0% O_2: 5 s	22	[21]
PtTFPP	n-Propyl-TriMOS/TFP-TriMOS	0% O_2 to 100% O_2: 3.7 s 100% O_2 to 0% O_2: 5.3 s	68.7	[22]
PtTFPP and dye entrapped core–shell nanoparticles (S-1)	Octyl-triEOS/TEOS	0% O_2 to 100% O_2: 1.3 s100% O_2 to 0% O_2: 18.6 s	166	Present study
PtTFPP and silica nanoparticles (S-2)	Octyl-triEOS/TEOS	0% O_2 to 100% O_2: 6.8 s100% O_2 to 0% O_2: 41.4 s	106	Present study

silica particle oxygen sensors when switching between fully oxygenated and fully deoxygenated environments, respectively. Note that in order to capture the true dynamic behavior of the sensor, the integration time for the CCD spectrometer was set to 30 ms. In general, the response time of optical oxygen sensors is defined as 95% of the response (or recovery) time when switching alternately between 100% oxygen and 100% nitrogen environments, respectively. The sensor doped with dye entrapped core–shell nanoparticles has a response time of 1.3 s when switching from nitrogen to oxygen and 18.6 s when switching from oxygen to nitrogen. The response time of the sensor doped with silica nanoparticles is 6.5 s when switching from nitrogen to oxygen and 31.6 s when switching from oxygen to nitrogen. Fig. 12(a) and (b) shows that the sensors produce a stable and reproducible fluorescence intensity signal as the sensing environment alternates between the two gaseous atmospheres. The sensors are thus suitable for practical measurement applications in which a reliable indication of the oxygen concentration is required.

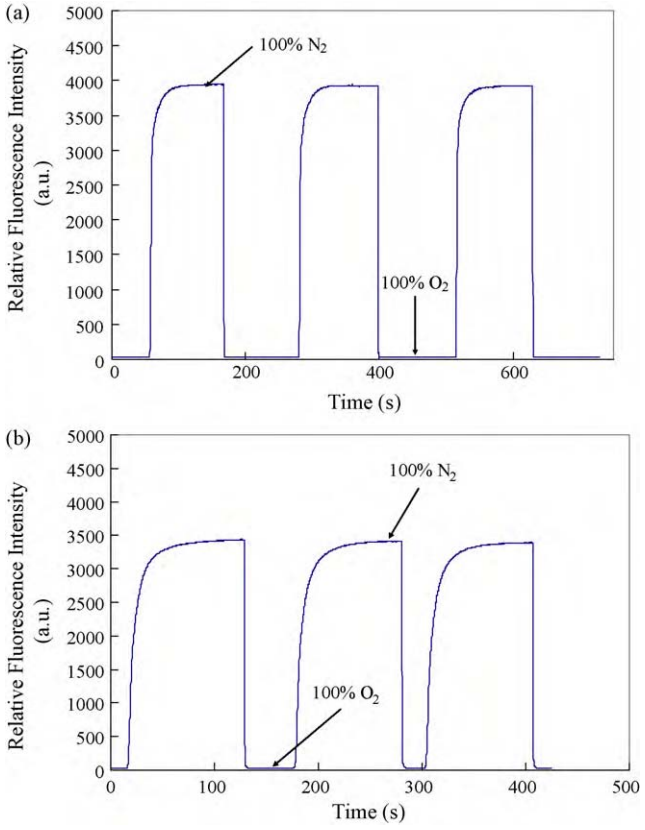

Fig. 12. Response characteristics of (a) PtTFPP-doped dye entrapped core–shell silica particle and (b) PtTFPP-doped silica particle sensors when switching alternately between 100% nitrogen and 100% oxygen.

4.4. Comparisons with existing O_2 sensors

Table 2 compares the performance characteristics of the proposed PtTFPP-doped oxygen sensors with those of representative quenchometric O_2 sensors presented in the literature comprising PtTFPP, PtOEP, or $Ru(dpp)_3^{2+}$ dyes embedded in various support matrices. Comparing the performance of the various sensors, it is apparent that sensors that use a platinum(II) complex as the sensing dye [19–21] have a significantly higher sensitivity than those using $Ru(dpp)_3^{2+}$ dye [16–18]. The proposed PtTFPP-doped dye entrapped core–shell silica particle oxygen sensor has the highest sensitivity (166) but its response time is slow. The improved sensitivity of the proposed sensor is due to the high surface-to-volume ratio of the dye entrapped core–shell silica nanoparticles, which improves the accessibility of the oxygen to the dye molecules and therefore enhances the quenching effect. The dye entrapped core–shell silica nanoparticles also increase the sensitivity of the oxygen sensor because a substantial number of aerial oxygen molecules penetrate the porous silica shell. The PtTFPP entrapped core–shell nanoparticles mixed with dye solution embedded in sol–gel matrix have a high surface-to-volume ratio and a high oxygen quenching efficiency, and thus enhanced sensitivity. Therefore, the core (PtTFPP)–shell (SiO_2) architecture plays an important role in this process.

5. Conclusions

This paper presented a highly sensitive optical fiber oxygen sensor based on platinum(II) complex (PtTFPP) and PtTFPP entrapped core–shell silica nanoparticles embedded in a sol–gel matrix. The experimental results show that the oxygen sensor has a linear response for oxygen concentrations in the range 0–20% and has a sensitivity of approximately 166 in the range 0–100%, which is considerably higher than those of typical optical oxygen sensors. The PtTFPP-doped dye entrapped core–shell silica particle sensor has a response time of 1.3 s when switching from pure nitrogen to pure oxygen environments and 18.6 s when switching in the reverse direction.

Dye entrapped core–shell nanoparticles are often used as bioimaging labels for living cells. Dye entrapped core–shell nanoparticles and fluorescent dye embedded in a sol–gel matrix were here used to enhance the sensitivity of an optical fiber oxygen sensor. The core–shell nanoparticles not only increase the surface area per unit mass in the sensing surface but also increase sensitivity because a substantial number of aerial oxygen molecules penetrate the porous silica shell. The localization of the dye is more prone to oxygen quenching. Thus, the proposed sensor can be used for highly sensitive applications.

Acknowledgement

The funding received from the National Science Council of Taiwan under grant NSC98-2811-E-006-057 is gratefully acknowledged.

References

[1] L.C. Clark Jr., Trans. Am. Soc. Artif. Intern. Organs 2 (1956) 41.
[2] D.B. Papkovsky, Sensors Actuators B: Chem. 29 (1995) 213.
[3] D.B. Papkovsky, Sensors Actuators B: Chem. 11 (1993) 293.
[4] J.N. Demas, B.A. Degraff, P.B. Coleman, Anal. Chem. 71 (1999) 793A.
[5] Y. Amao, Microchim. Acta 143 (2003) 1.
[6] C. Preininger, I. Klimant, O.S. Wolfbeis, Anal. Chem. 66 (1994) 1841.
[7] J.I. Peterson, R.V. Fitzgerald, D.K. Buckhold, Anal. Chem. 56 (1991) 62.
[8] E.R. Carraway, J.N. Demas, B.A. DeGraff, J.R. Bacon, Anal. Chem. 63 (1991) 337.
[9] B.G. Healey, D.R. Walt, Anal. Chem. 67 (1995) 4471.
[10] K. Tsukada, S. Sakai, K. Hase, H. Minamitani, Biosens. Bioelectron. 18 (2003) 1439.
[11] E. VanderDonckt, B. Camerman, R. Herne, R. Vandeloise, Sensors Actuators B: Chem. 32 (1996) 121.
[12] Y. Amao, T. Miyashita, I. Okura, J. Fluor. Chem. 107 (2001) 101.
[13] M.E. Lippitsch, J.P. Pusterhofer, M.J.P. Leiner, O.S. Wolfbeis, Anal. Chim. Acta 205 (1988) 1.
[14] S.K. Lee, I. Okura, Anal. Commun. 34 (1997) 185.
[15] S.K. Lee, I. Okura, Spectrochim. Acta A 54 (1998) 91.
[16] I. Klimant, F. Ruckruh, G. Libsch, C. Stangelmayer, O.S. Wolfbeis, Mikorchim. Acta 131 (1999) 35.
[17] A.N. Watkins, B.R. Wenner, J.D. Jordan, W.Y. Xu, J.N. Demas, F.V. Bright, Appl. Spectrosc. 52 (1998) 750.
[18] Y. Tang, E.C. Tehan, Z. Tao, F.V. Bright, Anal. Chem. 75 (2003) 2407.
[19] R.M. Bukowski, R. Ciriminna, M. Pagliaro, F.V. Bright, Anal. Chem. 77 (2005) 2670.
[20] S.K. Lee, I. Okura, Anal. Chim. Acta 342 (1997) 181.
[21] T.S. Yeh, C.S. Chu, Y.L. Lo, Sensors Actuators B: Chem. 119 (2006) 701.
[22] C.S. Chu, Y.L. Lo, Sensors Actuators B: Chem. 124 (2007) 376.
[23] J. Lin, C.W. Brown, Trace Trend Anal. Chem. 16 (1997) 200.
[24] B.D. MacCraith, C. McDonagh, G. OKeefe, E.T. Keyes, J.G. Vos, B. OKelly, J.F. McGilp, Analyst 118 (1993) 385.
[25] C. McDonagh, B.D. MacCraith, A.K. McEcoy, Anal. Chem. 70 (1998) 45.
[26] B.F. Lei, B. Li, H.R. Zhang, S.Z. Lu, Z.H. Zheng, W.L. Li, Y. Wang, Adv. Funct. Mater. 613 (2006) 1883.
[27] X.Y. Wang, C. Drew, S.H. Lee, K.J. Senecal, J. Kumar, L.A. Sarnuelson, Nano Lett. 11 (2002) 1273.
[28] S. Santra, K.M. Wang, R. Tapec, W.H. Tan, J. Biomed. Opt. 6 (2001) 160.
[29] H. Ow, D.R. Larson, M. Srivastava, B.A. Baird, W.W. Webb, U. Wiesner, Nano Lett. 5 (2005) 113.
[30] A.S. Ethiraj, N. Hebalkar, S. Kharrazi, J. Urban, S.P. Sainkar, S.K. Kulkarni, J. Lumines. 114 (2005) 15.
[31] F. Caruso, M. Spasova, V. Salgueirino-Maceira, L.M. Liz-Marzan, Adv. Mater. 13 (2001) 1090.
[32] B.H. Han, I. Manners, M.A. Winnik, Chem. Mater. 17 (2005) 3160.
[33] S.R. Guo, J.Y. Gong, P. Jiang, M. Wu, Y. Lu, S.H. Yu, Adv. Funct. Mater. 18 (2008) 872.
[34] J.R. Lakowicz, Principles of Fluorescence Spectroscopy, 2nd ed, Kluwer Academic/Plenum Press, New York, 1999 (Chapters 8 and 9).
[35] W. Xu, R.C. McDonough, B. Langsdorf, J.N. Demas, B.A. DeGraff, Anal. Chem. 66 (1994) 4133.
[36] J.N. Demas, B.A. DeGraff, W. Xu, Anal. Chem. 67 (1995) 1377.
[37] W. Stöber, A. Fink, E. Bohn, J. Colloid Interface Sci. 26 (1968) 62.
[38] J.H. Zhang, P. Zhan, Z.L. Wang, W.Y. Zhang, N.B. Ming, J. Mater. Res. 18 (2003) 649.
[39] H. Wang, M. Yu, C. Lin, X.M. Liu, J. Lin, J. Phys. Chem. C 111 (2007) 11223.
[40] Q. Chang, L.H. Zhu, C. Yu, H.Q. Tang, J. Lumines. 128 (2008) 1890.
[41] Z.L. Cheng, C.A. Aspinwall, Analyst 131 (2006) 236.
[42] S. Santra, B. Liesenfeld, C. Bertolino, D. Dutta, Z.H. Cao, W.H. Tan, B.M. Moudgil, R.A. Mericle, J. Lumines. 117 (2006) 75.
[43] R. Vacassy, R.J. Flatt, H. Hofmann, K.S. Choi, R.K. Singh, J. Colloid Interface Sci. 227 (2000) 302.